

**Electrocatalysis of Oxygen Evolution Reaction on SrIrO₃
grown using Molecular Beam Epitaxy**

A Thesis

Presented to the Faculty of the Graduate School

of Cornell University

In Partial Fulfillment of the Requirements for the Degree of

Master of Science

by

Runbang Tang

August 2015

© 2015 Runbang Tang

ABSTRACT

Electrochemical generation of oxygen via the oxygen evolution reaction (OER) is a key enabling step for many air-breathing electrochemical energy storage devices. Among the known OER catalysts, IrO_2 (Ir^{4+} : $5d^5$) is among the most active. In this thesis we present our measurement of the OER kinetics on single-crystal, epitaxial $\text{SrIrO}_3(100)$ synthesized using molecular-beam epitaxy on $\text{DyScO}_3(110)$. We find that by switching the host structure of the Ir^{4+} octahedra from edge-sharing rutile (IrO_2) to corner-sharing perovskite (SrIrO_3), the OER activity can increase by more than an order of magnitude. The dependence of the OER activity on the structure of Ir^{4+} suggests on the importance of the neighboring structure beyond a simple $\text{Ir}^{4+}\text{-O}_6$ unit in OER electrocatalysis. This finding highlights the need to incorporate the near-neighbor interaction consideration to the design of the future transition metal oxide electrocatalysts.

BIOGRAPHICAL SKETCH

Runbang Tang was born in Xian, China and got his bachelor degree from Harbin Institute of Technology in 2012, majoring in Materials Science and Engineering. During his bachelor degree, he was awarded National Merit Scholarship awarded by Chinese Ministry of Education and Magna Cum Laude by Harbin Institute of Technology. After completing his Bachelor degree, he came to Cornell University for Master of Science degree and joined Professor Jin Suntivich's group in September 2012. During his years in Cornell, he finished the project of studying the activity of SrIrO_3 for oxygen evolution reaction.

ACKNOWLEDGEMENTS

I would like to express my great thanks to my parents who gave me financial and moral support all the time and always helped me out when I was depressed with difficulties. They have always been companying me even we are apart for half of a world. I would like to show my great respect and gratitude to my advisor, Prof. Suntivich. Thanks him for giving me the opportunity to study on projects independently. He has been a nice advisor, a great instructor and a smart person to discuss science.

I am more than grateful to all my colleagues. It was them who made my everyday life interesting and colorful. Specifically I would like to show my thanks to Chris. He is always so helpful and we had lots of inspiring conversations. John spent countless hours teaching me English and introducing me to American society and cultures. He is one of most friendly guy I have ever seen. Chengyu Liu is also a nice colleague to get along with. I gained lots of help from her in labs as well as in everyday life. Thank Amit Bhatia, Anielli Pasqualeti and Ding-Yuan Kuo, all of whom have been really friendly and helpful. It's my great pleasure to work with these smart people under the dynamic group atmosphere.

I am happy to work with all the people mentioned above and my MS experience in Cornell has been really wonderful!

Table of Contents

Chapter 1 Introduction.....	1
1.1 Motivation & background.....	1
1.2 Proposed Mechanism for OER.....	4
1.3 Structural Data of Perovskites SrIrO ₃ and DyScO ₃	6
Chapter 2 Experimental Procedure.....	7
2.1 Molecular Beam Expitaxy (MBE) Synthesis.....	7
2.2 Electrochemical Characterizations.....	7
2.3 X-ray Diffraction.....	8
Chapter 3 Results and Discussion.....	9
3.1 XRD Diffraction.....	9
3.2 SrIrO ₃ Thin Film Stability.....	10
3.3 Electrical Contact & Charge Transfer.....	10
3.4 Cyclic Voltammetry in Ar Environment.....	12
3.5 Oxygen Evolution Reaction Performances.....	18
3.6 Effect of Thickness on the OER Activity of SrIrO ₃	19
3.7 Effect of Strain on the OER Activity of SrIrO ₃	20
Chapter 4 Summary and Outlook.....	23
REFERENCES.....	24

LIST OF FIGURES

Figure 1. Efficiency losses in typical fuel cell and electrolyzer systems.....	1
Figure 2. Binary metal oxide OER overpotential with enthalpy of transition from lower to higher oxides. Closed circles are results in acid media and open circles for alkaline.....	2
Figure 3. Exemplary X-ray diffraction (θ - 2θ scan) of a SrIrO ₃ film (40 formula-units) grown on DyScO ₃ (110). The pseudocubic reflections of SrIrO ₃ (denoted as 00L _p) confirm that the film attains a single phase SrIrO ₃	8
Figure 4. X-ray diffraction (θ - 2θ scan) of a SrIrO ₃ film (80 formula-units) grown on DyScO ₃ (110) before and after OER. The out-of-plane reflection remains after prolonged OER testing (~1 hour) of vigorous cycling, suggesting the stability of SrIrO ₃ for the OER. The diffraction spectra are offset for clarity.....	9
Figure 5. Impedance measurement of the three-electrode cell system. Electrical resistance of the system is taken to be the high frequency intercept, shown in orange arrow.....	10
Figure 6. Plot of the SrIrO ₃ CV in Ar-saturated 0.1M KOH electrolyte containing 5 mM Fe(CN) ₆ ^{3-/4-} at 10 mV/s scan rate, illustrating that the metallic nature of the electrode-electrolyte junction between 0.1M KOH and the SrIrO ₃ film.....	11
Figure 7. Cyclic voltammograms of SrIrO ₃ (100)/DyScO ₃ (110) in Ar-saturated 0.1M KOH at 50 mV/s and 200 mV/s scan rates.....	12

Figure 8. Plot of the SrIrO₃ CV in Ar-saturated 0.1M electrolyte of KOH, NaOH, and LiOH at (A) 50 mV/s scan rate and (B) 200 mV/s rate. We observed no noticeable difference for CV in different pH.....14

Figure 9. Plot of the SrIrO₃ CV in Ar-saturated KOH electrolytes at different pH at the potential scan rate of (A) 50 mV/s and (B) 200 mV/s shows a shift in the redox peak toward (C) higher potential with decreasing pH. As shown in Panel C (down-sided triangle, 50 mV/s scan rate, up-sided triangle, 200 mV/s scan rate), the shift in the redox peak with pH is scan-rate independent. We limit our study to pH > 12 as we found that pH ~12 near the limit of the SrIrO₃ stability. Panel (D) illustrates that the SrIrO₃ in pH 13 before and after an electrochemical test in pH 12.....16

Figure 10. (A) Cyclic voltammograms of SrIrO₃(100)/DyScO₃(110) in O₂-saturated 0.1 M KOH at 10 mV/s. (B) Tafel plot of the OER kinetics from (A). The OER kinetics of IrO₂(110) grown on MgO(100) single crystal is shown for comparison (*Ref. 18). The OER kinetics for SrIrO₃ changes less than 5 mV from the 1st scan to steady-state. The steady-state data is shown in the Figure. The shaded gray area represents the standard deviation for three independent measurements.....18

Figure 11. (A) Plot of the SrIrO₃ CV in O₂-saturated KOH electrolytes at different pH at 10 mV/s scan rate. (B) The OER activities of the SrIrO₃ as a function of proton concentration, showing a linear dependence with [H⁺]. The red line serves only as a visual guide to the observed activity trend.....19

Figure 12. Tafel plot for the OER activities measured via chronoamperometry for 40 formula-units (red triangles) and 80 formula-units SrIrO₃ (blue circles). The thicker,

80 formula-units SrIrO₃'s higher OER activity is likely from to the rougher surface.....20

Figure 13. SrIrO₃ OER activities under different potentials with different strain at 40 f.u. and 80 f.u. thicknesses respectively. (A) 1.48V vs RHE. (B) 1.53V vs RHE. (C) 1.58V vs RHE.....21

Figure 14. Calculated free energy of the OER intermediates for IrO₂ and SrIrO₃, solid line: at 1.23V vs. RHE, dashed line: at 0V vs. RHE, dotted line: at the thermodynamic overpotential. All calculations use GGA-RPBE with (A) $U = 0$ eV, (B) $U = 1$ eV, and (C) $U = 2$ eV.....22

1.1 Motivation & Background

The kinetics of the oxygen evolution reaction (OER, in alkaline: $4\text{OH}^- \rightarrow \text{O}_2 + 2\text{H}_2\text{O} + 4\text{e}^-$) is central to the efficiency of many air-breathing electrochemical energy storage systems, including solar- and electricity-driven electrolysis^{1,2} and rechargeable metal-air batteries^{3,4}. The role that the OER kinetics plays is shown in Figure 1 for a typical water electrolyzer system¹. The discovery of an OER catalyst that can accelerate the OER kinetics and decrease the OER overpotential can serve as a vehicle for increasing the water splitting efficiency and thereby reducing cost.

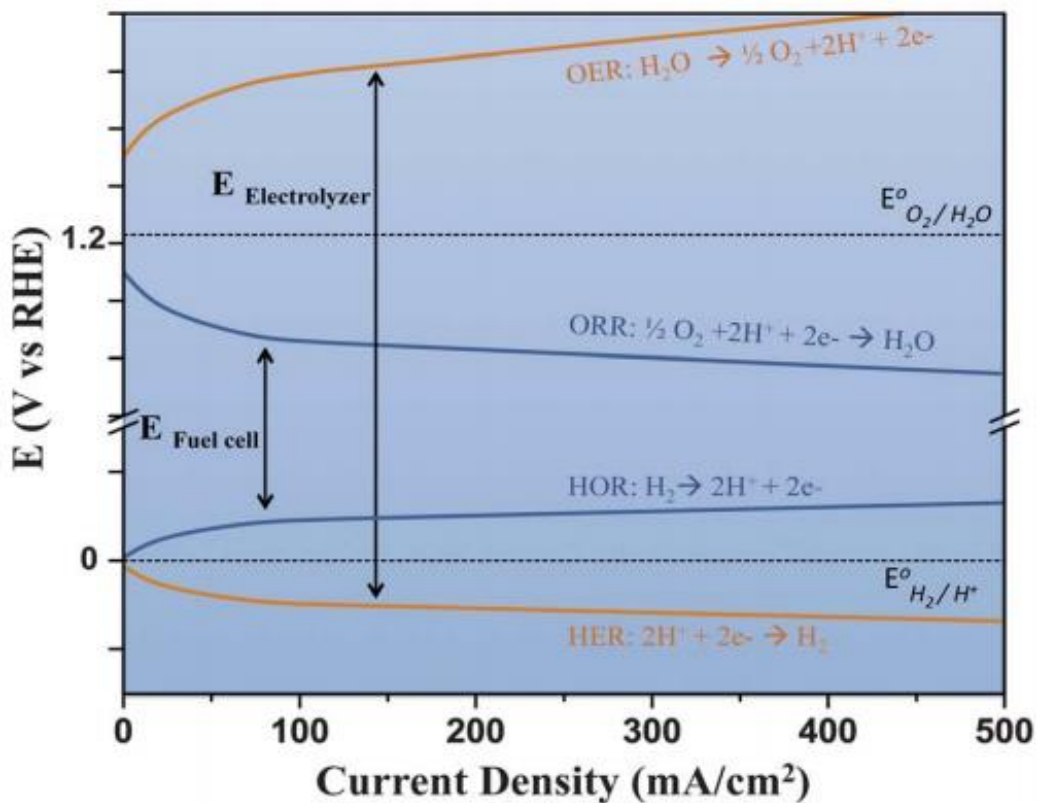


Figure 1. Efficiency losses in typical fuel cell and electrolyzer systems. Figure adapted from Ref. 1

In an effort to find superior materials as OER catalysts to decrease the activation overpotential, Trasatti has surveyed the OER kinetics over a large number of transition metal oxides⁵ and identified IrO₂ and RuO₂ as the most active binary OER electrocatalysts (Figure 2). Decades later, using *ab initio* calculations, Norskov and Rossmeisl have suggested that the high OER activities of these precious-metal oxides are due to the stable formations of the intermediates during the OER⁶⁻⁸. Using the scaling relation, they also establish the surface oxygen binding as a descriptor to the OER activity.

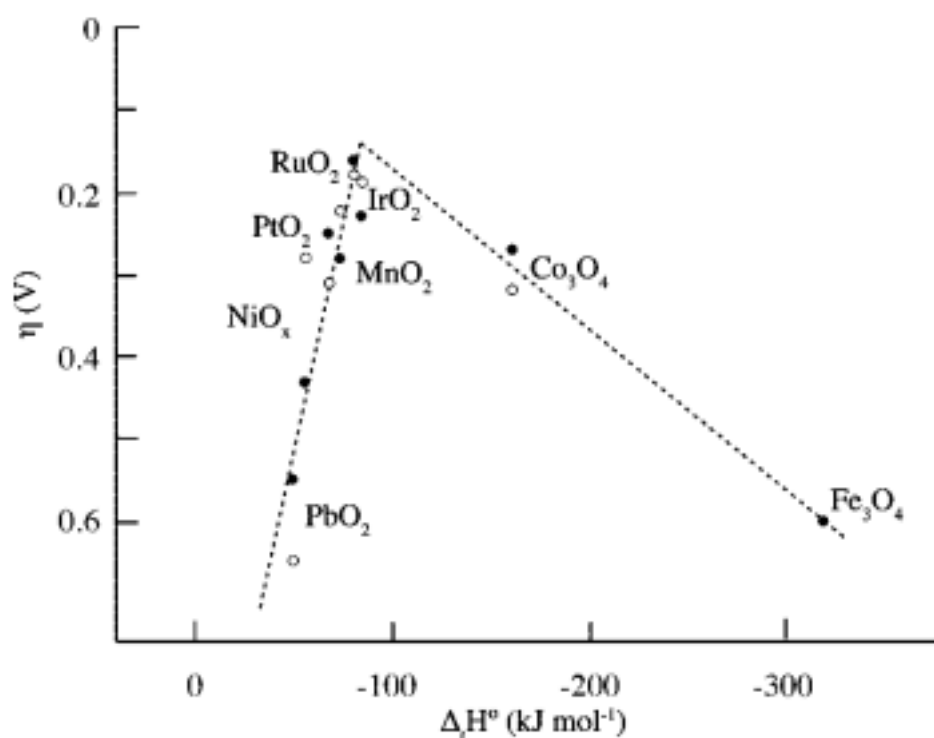


Figure 2. Binary metal oxide OER overpotential with enthalpy of transition from lower to higher oxides.

Closed circles are results in acid media and open circles for alkaline^{5,50}. Figure adapted from Ref. 50.

Inspired by this finding, intensive efforts have been spent on identifying strategies for controlling the surface oxygen-binding energy by using, for example, transition

metal substitutions^{9,10}, structural engineering^{11,12} and support interactions^{13,14}. Although these efforts have led to many successful developments of new OER catalysts^{9,11}, the studies have largely focused on polydisperse-catalyst oxides. This reliance on the polydisperse materials complicates the process of connecting the surface structure with the electrochemical mechanism as there can be different terminations and/or multiple phases present within the same catalytic material. With the exception of SrRuO₃, which was found to be unstable for the OER¹⁵, very few well-defined, single-crystal *5d* transition metal oxides surfaces, notably IrO₂ and RuO₂, have been studied as OER catalysts^{16,17}. This thesis focuses on investigating the properties of a new, well-defined, single-crystal *5d* perovskite-oxide SrIrO₃ catalyst synthesized via molecular-beam epitaxy (MBE). We find that the OER activity of the SrIrO₃ is more than an order of magnitude higher than IrO₂, despite both SrIrO₃ and IrO₂ sharing the same Ir⁴⁺O₆ octahedra moiety. In addition, the well-defined nature of the MBE-grown catalyst also opens up an avenue to connect between the OER and the *ab initio* calculations. Density function theory (DFT) results reveal that to reproduce the experimental observation of SrIrO₃'s superior OER activity over IrO₂, the OER pathway on SrIrO₃ does not follow the conventional hydroxide deprotonation or oxygen electrochemical bond formation⁶⁻⁸.

SrIrO₃ has received widespread attention as a material with a delicate balance between the spin-orbit interaction, the Coulomb interaction, and the *5d* electron delocalization^{18,19}. Metastable by nature, realizing the perovskite phase of SrIrO₃

generally requires a high-temperature, high-pressure synthesis condition^{20,21}. The growth of single-crystal SrIrO₃ thin films with high structural perfection was recently realized with MBE with low-pressure ozone as an oxidant^{22,23}. Through angle-resolved photoemission spectroscopy (ARPES) experiments, it was additionally shown that SrIrO₃ is a narrow-band semimetal as a result of the spin-orbit interaction that breaks the degeneracy of the t_{2g} orbitals into the $J_{eff} = 1/2$ and $3/2$ states²³. This bandwidth narrowing, as induced by the spin-orbit interaction (SOI), leads to a non-negligible on-site Coulomb interaction that turns SrIrO₃ into a correlated semimetal¹⁹. From the OER catalysis perspective, SrIrO₃ is an interesting $5d$ transition metal oxide compound to examine, especially in comparison to IrO₂. Notably, although both share a similar electronic configuration (Ir⁴⁺: $5d^5$), the semimetal SrIrO₃ exhibits an electronic correlation, in comparison to IrO₂ that is an uncorrelated metallic oxide²⁴⁻²⁶. Many theoretical investigations had discussed the importance and the possibility of using the Coulomb interaction to tune the OER activity^{27,28}. Examining the OER activity of SrIrO₃ can therefore provide insights into the question of whether the OER activity of the Ir⁴⁺O₆ depends on the material structure, perovskite for SrIrO₃ and rutile for IrO₂, and the role of the electron correlation on the OER activity on transition metal oxide catalysts.

SrIrO₃ has an orthorhombic perovskite structure (with the following structural data: $a = 5.591\text{\AA}$, $b = 7.882\text{\AA}$, and $c = 5.562\text{\AA}$ ²⁰.) To approximate the SrIrO₃ structure grown epitaxially on DyScO₃, a pseudocubic structure is adopted. Within this

framework, the lattice parameter is $a_0 = 3.942 \text{ \AA}$. This represents $\sim 0.05\%$ strain with respect to the DyScO_3 perovskite substrate in an equivalent pseudocubic approximation (the DyScO_3 perovskite's pseudocubic lattice parameter is approximately 3.945 \AA). At this strain number, we can approximate one unit cell dislocation per 200 unit cells. Our focus is on SrIrO_3 with thickness less than 80 unit cells. A structural perfection can therefore be expected.

Chapter 2

Experimental Procedure

2.1 Molecular Beam Epitaxy (MBE) Synthesis.

SrIrO₃ was grown by MBE on single-crystal DyScO₃(110) (CrysTec) using a distilled ozone (O₃) oxidant at the background pressure of 10⁻⁶ Torr. Based on the structural data for SrIrO₃²⁰ and DyScO₃²², we estimate ~0.05% strain for the SrIrO₃(100) film grown on DyScO₃(110).

2.2 Electrochemical Characterizations.

Electrical contacts were made in the same protocol as reported previously^{16,38}. First, corner front surface of the sample was scratched using a diamond tip. Then Gallium-Indium eutectic was spread evenly onto the scratched parts. A Titanium wire was contacted to the scratched surface with silver paste. The back and sides of the sample as well as contact part were covered with chemically inert epoxy to ensure that only the catalytic active surface was exposed to the electrolyte. All electrochemical characterizations were conducted in a three-electrode glass cell with a potentiostat (Bio-Logic). The reference electrode was a Ag/AgCl redox couple in saturated KCl solution, calibrated to the H₂ redox in the same electrolyte, and the counter electrode was Pt wire. The electrolyte/cell-resistance-free potentials were obtained by subtracting the product of current and resistance from experimental observed

potentials. Electrolyte/cell resistance was determined using the high frequency intercept of real resistance from impedance measurement.

OER electrocatalysis was conducted in KOH solutions, prepared from Milli-Q water (Millipore) with KOH pellets (Sigma-Aldrich, 99.995%) under O₂ saturated environment. Capacitance free CV curves were obtained by averaging the forward and backward scans. The OER activity was evaluated from both CV (at 10 mV/s sweep rate from 1.1V to 1.7V vs. RHE) and chronoamperometry. The shaded error bars represent standard deviations for at least three independent measurements. [Fe(CN)₆]^{3-/4-} measurements were performed in Ar-saturated 0.1 M KOH solution with 5 mM K₄Fe(CN)₆·3H₂O (SigmaAldrich, 99.99%) and K₃Fe(CN)₆ (Sigma-Aldrich, 99%). We did not observe any significant degradation throughout the electrochemical testing. The CV did not grow with time and therefore does not suggest an amorphization of the catalyst sample⁴⁸.

2.3 X-ray Diffraction

The X-ray diffraction (θ -2 θ scan) graph of the sample was obtained using Rigaku SmartLab in the Cornell Center for Materials Research (CCMR). The X-ray diffraction uses the Cu K α emission, which has an X-ray wavelength of 0.157 nm.

3.1 XRD diffraction

XRD of SrIrO₃ thin films grown on DyScO₃ substrates with 40 functional unit (about 16 nm thickness) is shown in Figure 3. The diffraction data suggests that the thin films are epitaxially grown on the substrates. Notably, the peaks of the substrates and peaks of SrIrO₃ nearly overlap, indicating the consistency of the pseudocubic approximation on the SrIrO₃ thin film. Kiessig fringes indicate that the thin films are smooth and thickness is calculated to be 16 nm using the spacing between the two adjacent fringes ($\Delta\theta$, with $2d \sin \Delta\theta = \lambda$).

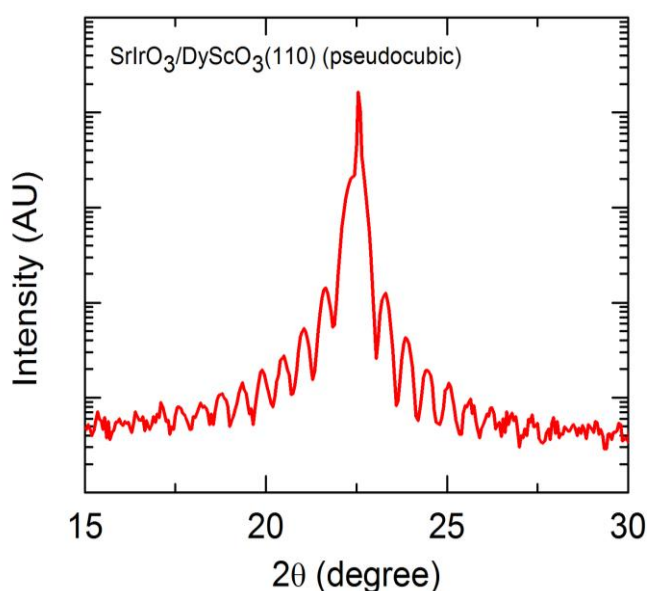


Figure 3. Exemplary X-ray diffraction (θ - 2θ scan) of a SrIrO₃ film (40 formula-units) grown on DyScO₃(110). The pseudocubic reflections of SrIrO₃ (denoted as 00L_p) confirm that the film attains a single phase SrIrO₃.

3.2 SrIrO₃ thin film stability

To determine the SrIrO₃ stability during the OER in alkaline solutions, comparison between the XRD of SrIrO₃ thin film of 80nm thickness before the OER and after OER is shown in Figure 4. The consistency of the XRD graphs before and after the OER supports the stability of the SrIrO₃ thin films during the OER.

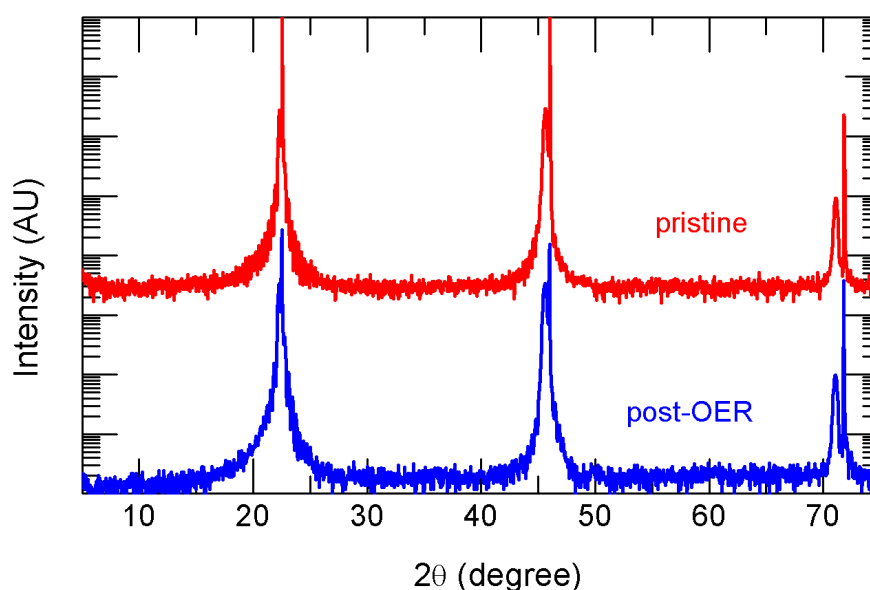


Figure 4. X-ray diffraction (θ - 2θ scan) of a SrIrO₃ film (80 formula-units) grown on DyScO₃(110) before and after OER. The out-of-plane reflection remains after prolonged OER testing (~1 hour) of vigorous cycling, suggesting the stability of SrIrO₃ for the OER. The diffraction spectra are offset for clarity.

3.3 Electrical Contact & Charge Transfer

The electrical contact was obtained using the procedures described in chapter 2. The impedance measurement under various potentials is shown in Figure 5. Electrolyte/cell resistance will not change with potentials and was determined using

the high frequency intercept of real resistance from impedance measurement. In our system, the electrolyte/cell resistance was measured to be around 183 Ω . This number is notably lower than the fully metallic catalyst (usually $\sim 40\text{-}45 \text{ }\Omega$). At moment, we assign this resistance to the internal resistance within the semi-metallic SrIrO₃ films. Future examinations to understand the ohmic contributions from contacts, films, and interfaces would be essential to optimize this resistance.

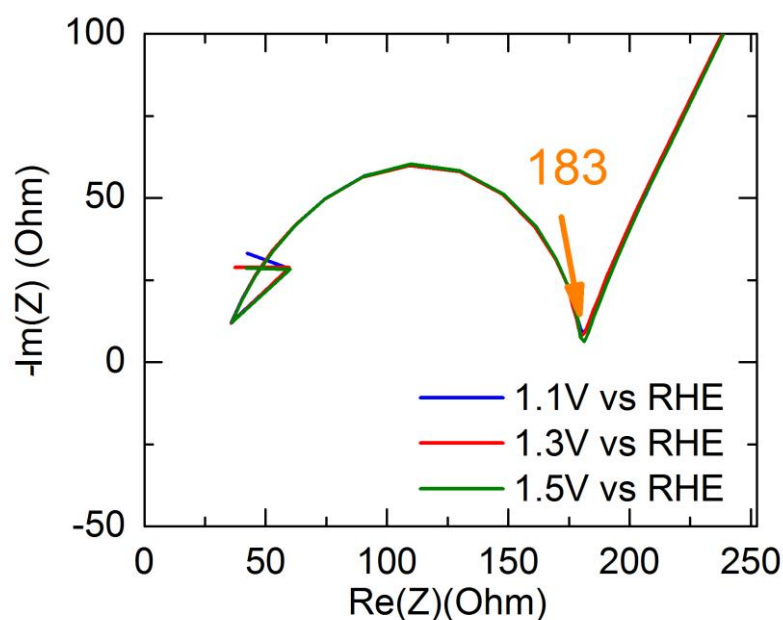


Figure 5. Impedance measurement of the three-electrode cell system. Electrical resistance of the system is taken to be the high frequency intercept, shown in orange arrow.

[Fe(CN)]^{3-/4-} measurements were shown in Figure 6. The [Fe(CN)]^{3-/4-} redox kinetics is based on an outer shell electron transfer and is presumed to be kinetically fast. Because of this property, we are used as a probe for the interface charge transfer resistance. As shown in Figure 6, the difference in the oxidation and reduction curves

reflects the ease of electron transfer from the electrode surface to the redox couple in the electrolyte³⁸. The quasi-reversible kinetics of the redox reaction of $[\text{Fe}(\text{CN})_6]^{3-/4-}$ occurs on the SrIrO_3 thin film; the separation between the cathodic and the anodic scans is observed to be $\sim 0.1\text{V}$. Although this likely indicates that the influence of the kinetics on the cyclic voltammogram, it is seen that the junction is not rectifying, unlike what has been observed for LaMnO_3 ³⁸.

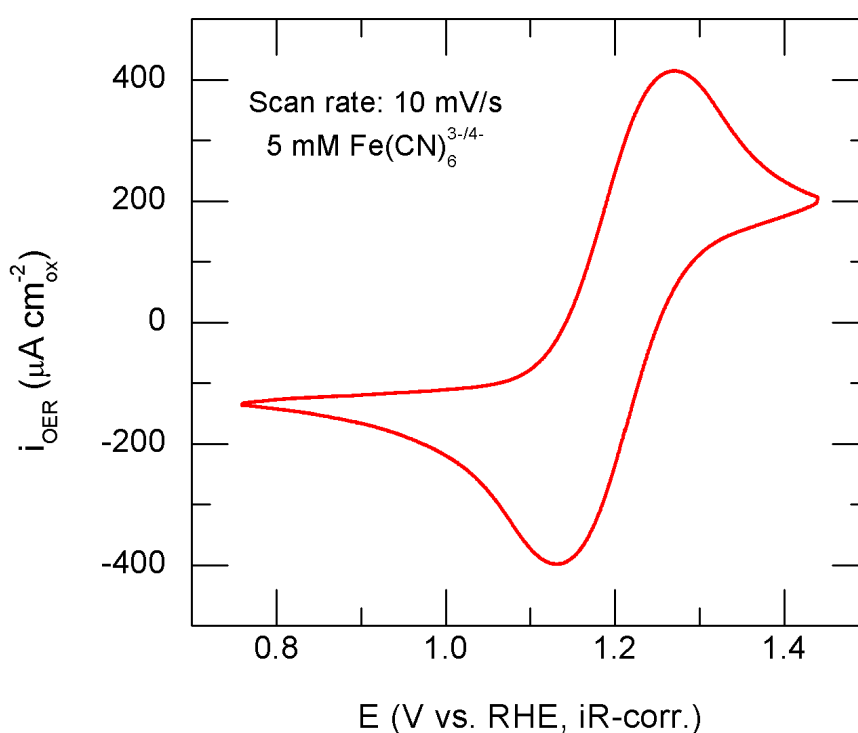


Figure 6. Plot of the SrIrO_3 CV in Ar-saturated 0.1M KOH electrolyte containing 5 mM $[\text{Fe}(\text{CN})_6]^{3-/4-}$ at 10 mV/s scan rate, illustrating that the metallic nature of the electrode-electrolyte junction between 0.1M KOH and the SrIrO_3 film.

3.4 Cyclic Voltammetry in Ar Environment

In Figure 7, we show the cyclic voltammogram of the $\text{SrIrO}_3(100)$ grown on $\text{DyScO}_3(110)$ in 0.1 M KOH. The presence of a reversible peak near 0.6 V vs.

reversible hydrogen electrode (RHE) is notable; this peak does not appear in the rutile IrO_2 catalyst in either poly-crystalline, (100)-, (110)-oriented¹⁶, or certain amorphous iridate films²⁹; however, it is seen in hydrated iridium oxide films as an $\text{Ir}^{\text{III}}/\text{Ir}^{\text{IV}}$ redox^{30,31}. It is unlikely that the SrIrO_3 film transforms into hydrated iridium oxides as (1) not all the electrochemical features for SrIrO_3 and the hydrated iridium oxide films are the same (for example, the CVs of the hydrated iridium oxide films go to zero at 0.2 V vs. RHE, whereas the SrIrO_3 does not), (2) the X-ray diffraction result shows virtually the same reflection features before and after OER (see Supporting Information), and (3) most importantly, the integrated charge underneath the CV curve of SrIrO_3 (from Figure 7) is consistent with a surface process ($215 \mu\text{C}/\text{cm}^2$ or $\sim 2.1e^-$ per surface Ir) unlike the hydrated iridium oxide film, where the electrochemical process can penetrate deep inside the film (up to $40 \text{mC}/\text{cm}^2$)^{31,32}. When considering that the CV curve of SrIrO_3 in Figure 7 likely contains more than one redox peak along with the double-layer capacitance, it is likely that only top layer of SrIrO_3 participates in the redox process. It is possible, however, that the reduced interaction between the corner-sharing Ir (in comparison to the edge-sharing Ir in rutile IrO_2) renders SrIrO_3 chemically similar to the hydrated iridium oxide films, where each individual Ir sites are more isolated than crystalline rutile IrO_2 .

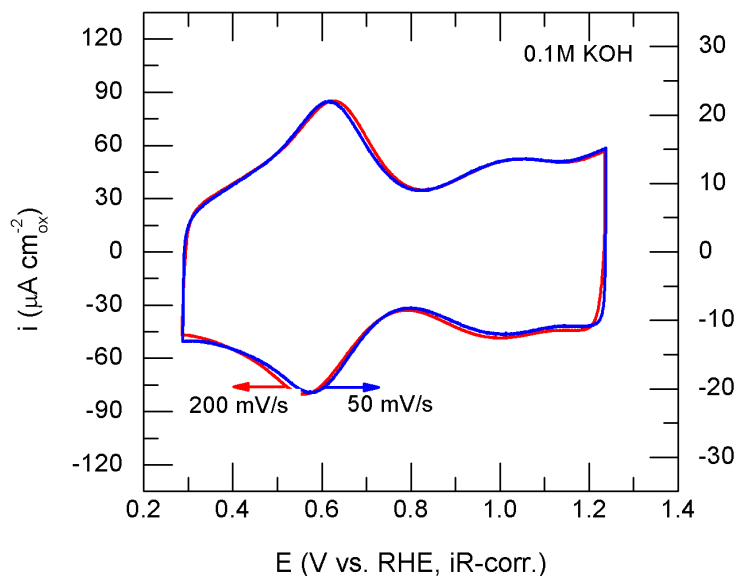


Figure 7. Cyclic voltammograms of SrIrO₃(100)/DyScO₃(110) in Ar-saturated 0.1M KOH at 50 mV/s and 200 mV/s scan rates.

To further unveil the origin of the redox peak, we compare the cyclic voltammetry (CV) of SrIrO₃/DyScO₃ in LiOH, NaOH, and KOH electrolytes (shown in Figure 8 A & B). We observed no noticeable difference in all three electrolytes. This observation is different from Pt, where the water oxidation peak ($\text{Pt} + \text{OH}^- \rightarrow \text{Pt-OH} + \text{e}^-$) that occurs at a similar electrochemical potential has been observed to change with electrolyte cations³³. Likely, this reflects that the surface-cation interactions are approximately the same for both the reduced- and the oxidized-states on SrIrO₃ (hence preserving the energy difference)³⁴. One assignment that is consistent with this possibility is the redox of the Ir-OH site ($\text{Ir-OH} + \text{e}^- \rightarrow \text{Ir-OH}^-$), where both Ir-OH⁻ and Ir-OH (including Ir-O⁻ that is in equilibrium with Ir-OH) have approximately the same magnitude of the surface-cation interaction. This assignment is in agreement with the DFT calculation,

which suggests the electrochemical adsorption of Ir-OH occurs well below 1.23 V vs. RHE (more detailed discussion below).

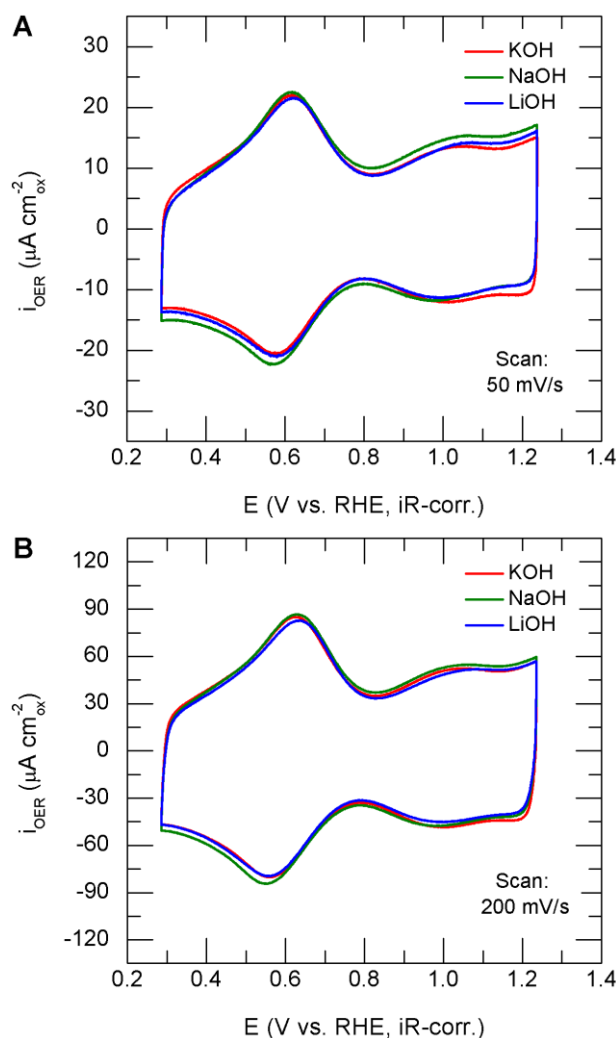
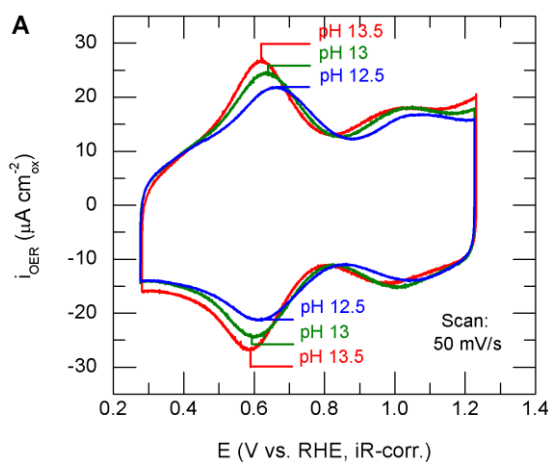


Figure 8. Plot of the SrIrO₃ CV in Ar-saturated 0.1M electrolyte of KOH, NaOH, and LiOH at (A) 50 mV/s scan rate and (B) 200 mV/s rate. We observed no noticeable difference for CV in different pH.

We further compare the CV of SrIrO₃/DyScO₃ in a series of alkaline pH (Figure 9). We observe that the redox peak maintains the reversibility but shifts to higher electrochemical potential (referenced to the RHE scale) and appears more broadened with acidic pH. Koper and co-workers have suggested that the origin of the pH dependence of the surface adsorption peak (with respect to the RHE scale) can be from

the mixed (but concerted) proton-electron/electron transfer nature of the surface electro-adsorption^{35,36}. We hypothesize that this is the case for SrIrO₃, where the acid-base equilibrium between Ir-OH and Ir-OH⁻ translates to a surface electro-adsorption that does not have a 1:1 stoichiometry between proton and electron, and hence an anomalous pH dependence. In line with this acid-base argument, we hypothesize that the broadening of the redox peak stems from the changing nearest-neighbor interactions as a result of the shift in the Ir-OH/Ir-O⁻ equilibrium with pH and electrochemical potential. The observed shift in the redox peak with pH moves in the same direction as the hydrated iridium oxide but, interestingly, in the opposite direction as the hydrogen electro-adsorption peaks on Pt, which systematically shift to higher electrochemical potentials with increasing pH³⁵⁻³⁷. We emphasize that our assignments are meant only for qualitative discussions; the exact origin of the SrIrO₃ CV peak is admittedly, still speculative. Further *in situ* surface spectroscopy is essential to unravel the interaction at the SrIrO₃-electrolyte interface.



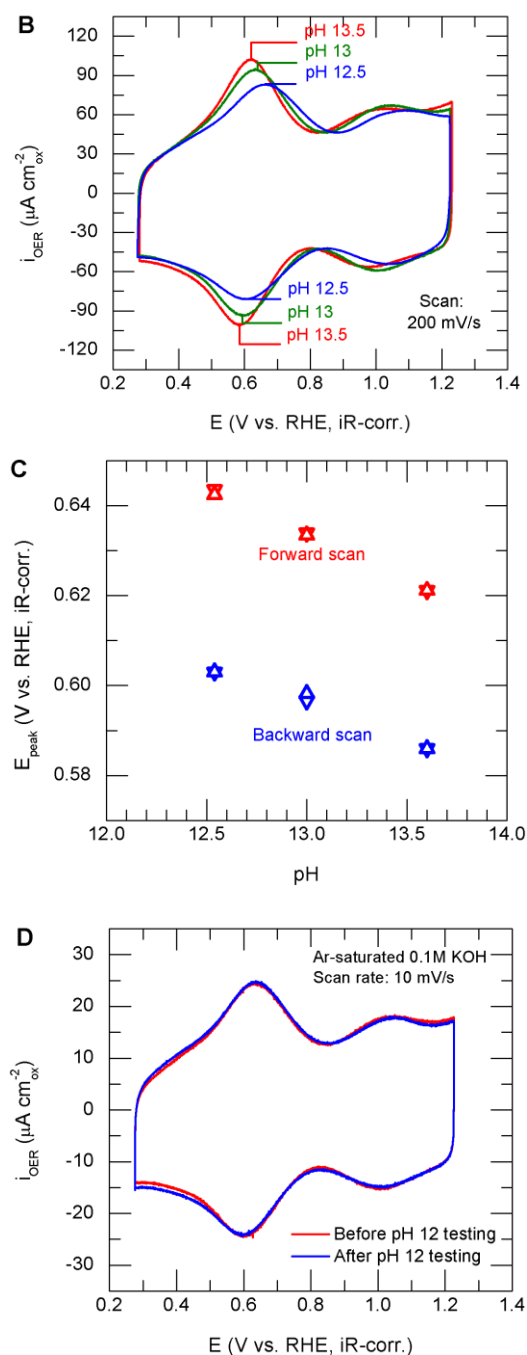


Figure 9. Plot of the SrIrO₃ CV in Ar-saturated KOH electrolytes at different pH at the potential scan rate of (A) 50 mV/s and (B) 200 mV/s shows a shift in the redox peak toward (C) higher potential with decreasing pH. As shown in Panel C (down-sided triangle, 50 mV/s scan rate, up-sided triangle, 200 mV/s scan rate), the shift in the redox peak with pH is scan-rate independent. We limit our study to pH > 12 as we found that pH ~12 near the limit of the SrIrO₃ stability. Panel (D) illustrates that the SrIrO₃ in pH 13 before and after an electrochemical test in pH 12.

3.5 Oxygen Evolution Reaction performances

The OER kinetics for SrIrO₃ in 0.1M KOH is shown in Figure 10A. Assuming that the roughness factor ($\text{cm}^2_{\text{ox}}/\text{cm}^2_{\text{geo}}$) is ~ 1 ^{16,38}, the OER kinetics for SrIrO₃ is at least an order of magnitude higher than previously reported IrO₂ catalysts (Figure 10B, an OER kinetics estimate on IrO₂(110), the low surface-energy termination of the rutile structure from Ref. 18, is included as a reference). We observe that the OER on SrIrO₃ exhibits a lower Tafel slope (~ 40 mV/decade, extracted from the low current density regime, < 0.5 mA/cm², to minimize artifacts from the electrolyte-resistance correction) than rutile IrO₂ and RuO₂ (~ 60 mV/decade)^{16,39}. In the single-electron Butler-Volmer form, this Tafel slope would translate to a rather unphysical anodic transfer coefficient (α) of 1.5. Clearly, this is indicative that a potential-dependent surface coverage^{40,41} or the possibility of a multi-electron process must be at play⁴². To further examine the OER electrokinetics, we compare the OER activities in a series of alkaline pH. We limit our experimental testing to electrolytes with pH > 12 , where KOH can sufficiently buffer the solution, and to the potential region where the electrolyte-resistance correction (ohmic) is smaller than the measurement error to minimize artifacts. We find that the OER activity decreases linearly with the proton concentration (shown in Figure 11). This inverse, first-order proton activity could be due to either the possibility of a mixed (but concerted) proton-electron/electron transfer rate-limiting oxidation step or the surface coverage interference (by either poisoning or non-covalent interaction.)

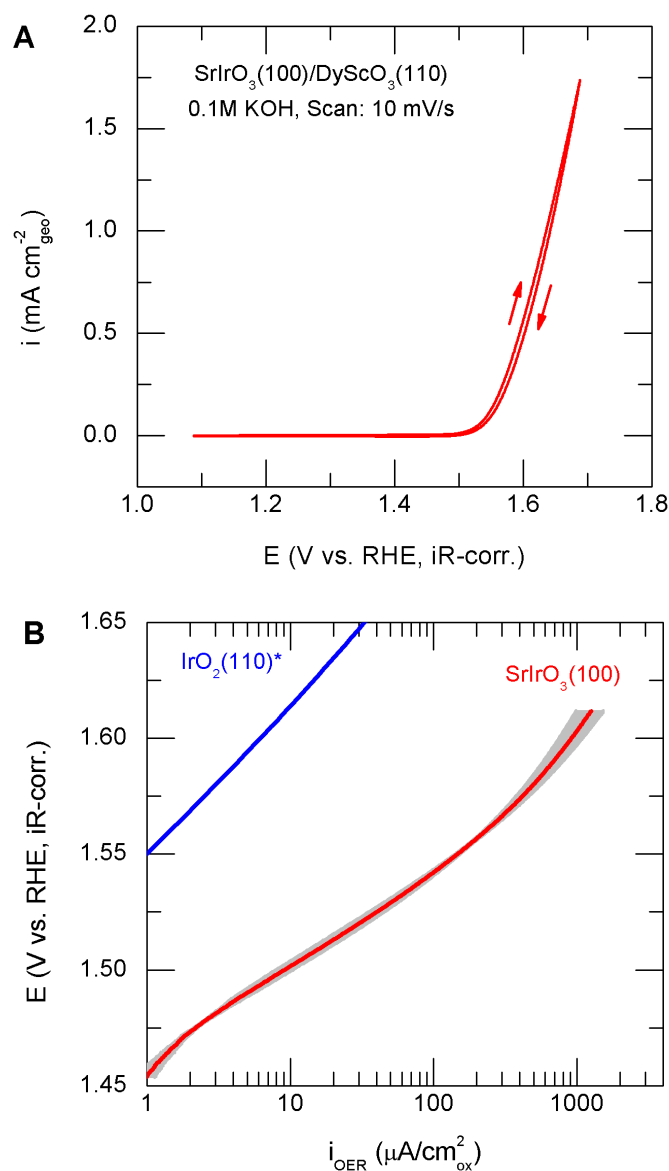


Figure 10. (A) Cyclic voltammograms of SrIrO₃(100)/DyScO₃(110) in O₂-saturated 0.1 M KOH at 10 mV/s. (B) Tafel plot of the OER kinetics from (A). The OER kinetics of IrO₂(110) grown on MgO(100) single crystal is shown for comparison (*Ref. 18). The OER kinetics for SrIrO₃ changes less than 5 mV from the 1st scan to steady-state. The steady-state data is shown in the Figure. The shaded gray area represents the standard deviation for three independent measurements.

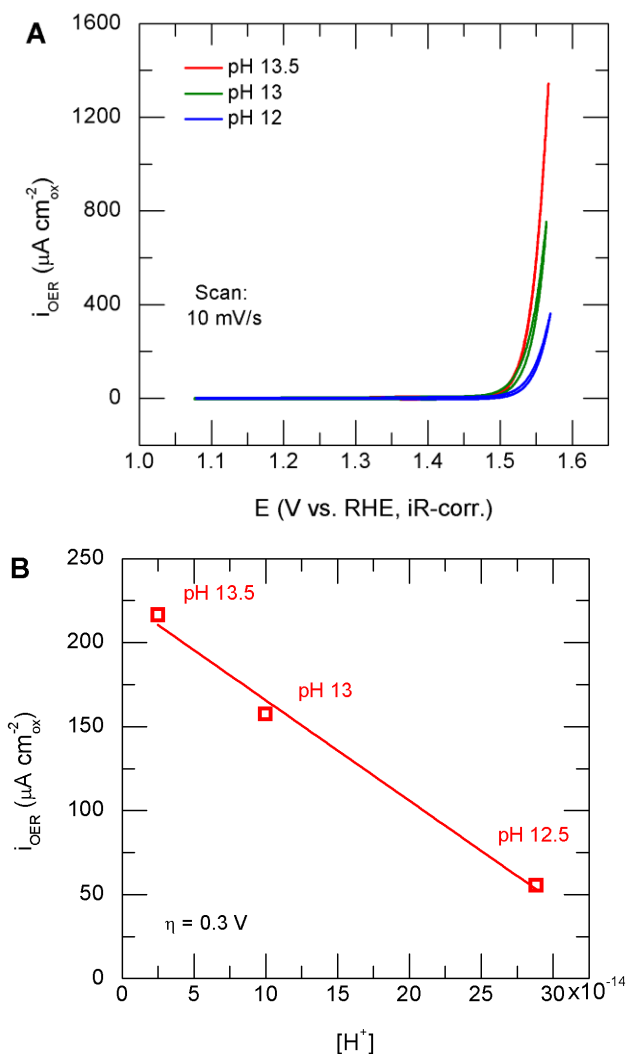


Figure 11. (A) Plot of the SrIrO₃ CV in O₂-saturated KOH electrolytes at different pH at 10 mV/s scan rate. (B) The OER activities of the SrIrO₃ as a function of proton concentration, showing a linear dependence with [H⁺]. The red line serves only as a visual guide to the observed activity trend.

3.6 Effect of Thickness on the OER Activity of SrIrO₃

We further examine whether the OER activity could be influenced by the thickness of the SrIrO₃ film. Stoerzinger and co-workers have previously reported the interference from the substrate the electrocatalytic activity³⁸. To address this possibility, we compared the OER activities for SrIrO₃ thin films with 40 f.u.(~16 nm) and 80 f.u. (~32 nm) thicknesses. As show in Figure 12, comparable OER activities

were observed, suggesting little dependence of the OER activities on the thickness of the SrIrO₃ thin film (thickness larger than 16 nm). The slight difference in activities might come from the roughness difference.

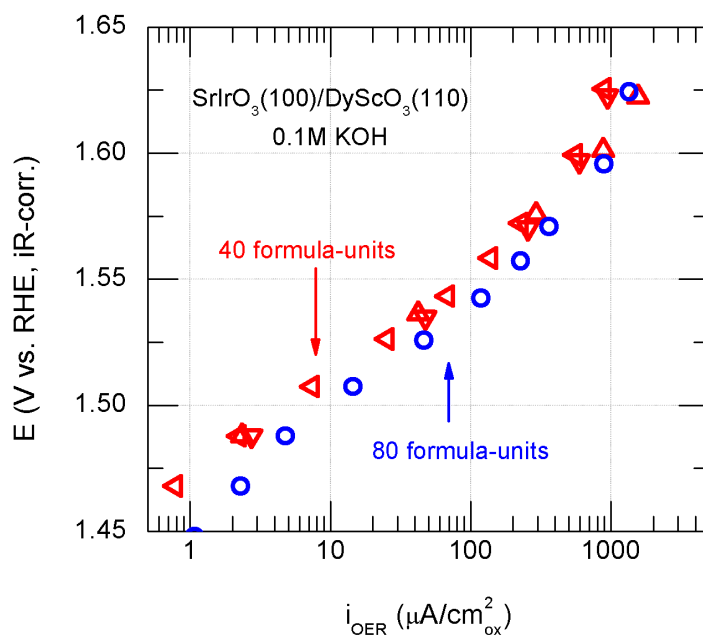


Figure 12. Tafel plot for the OER activities measured via chronoamperometry for 40 formula-units (red triangles) and 80 formula-units SrIrO₃ (blue circles). The thicker, 80 formula-units SrIrO₃'s higher OER activity is likely from to the rougher surface.

3.7 Effect of Strain on the OER Activity of SrIrO₃

The ability to synthesize transition metal oxide films with pinpoint-strain accuracy has long been a cornerstone of the MBE²². We take advantage of this MBE synthesis to preliminarily evaluate the effect of strain on the OER activity of SrIrO₃. A preliminary result on the strain in the OER catalysis on SrIrO₃ is shown in Figure 13, illustrating the SrIrO₃ OER kinetics with different SrIrO₃ strain achieved by using

substrates with smaller lattice parameter than DyScO₃ (e.g. SrTiO₃(100) and (LaAlO₃)_{0.3}(Sr₂AlTaO₆)_{0.7} “LSAT” (100)). At present, we cannot conclude the role of strain on the OER activity for SrIrO₃ with 80 formula unit (f.u.) thickness. We note however, that for 40 f.u.-thick SrIrO₃, the OER activity appears strain-independent. Further study is essential to conclude the dependence of OER activities on strain.

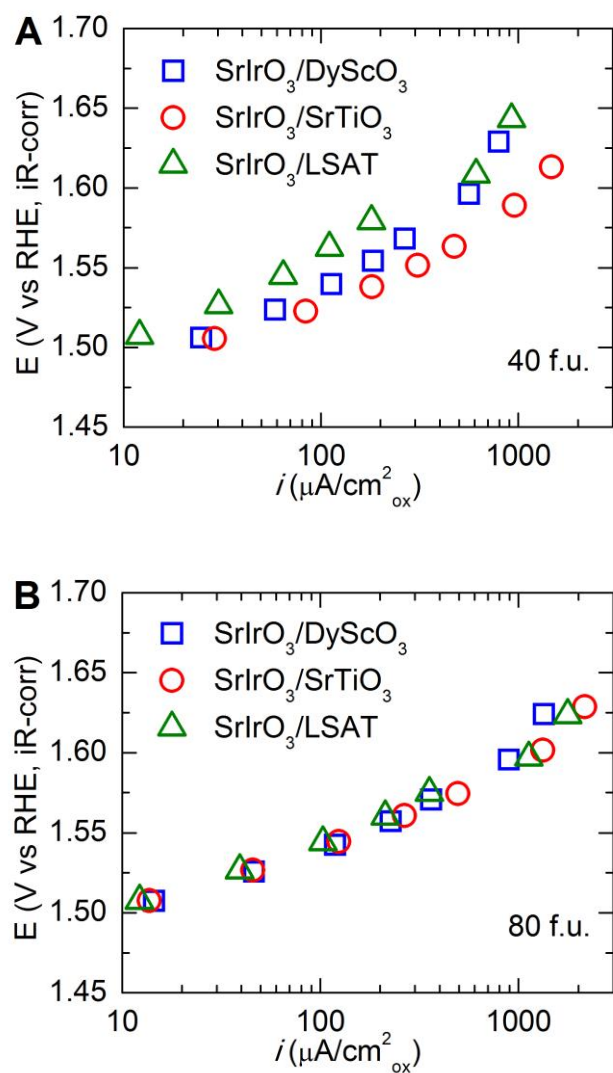


Figure 13. SrIrO₃ OER activities with different strain at 40 f.u. and 80 f.u. thicknesses respectively. (A) 40 f.u. (B) 80 f.u.

To understand the origin of the SrIrO₃ electrochemical behaviors, our collaborator has further conducted a DFT calculation to unveil the difference between IrO₂ and SrIrO₃. The employed formalism follows the approach developed by Norskov using a hydrogen redox to constrain the reference to estimate the electrochemical energy^{6,7,43}. The O*, OH*, and OOH* energetics on SrIrO₃ and IrO₂ slabs are shown in Figure 14. The calculation reveals that SrIrO₃ requires more thermodynamics overpotential than IrO₂ for the OER regardless of the *U* correction; with or without the *U* correction, our calculation would predict that IrO₂ requires less thermodynamics overpotential than SrIrO₃, which is opposite from our experimental observation. The only way we can instill meaning to the calculated surface energetics of SrIrO₃ is to assume that the OER occurs via a different pathway⁴⁰⁻⁴².

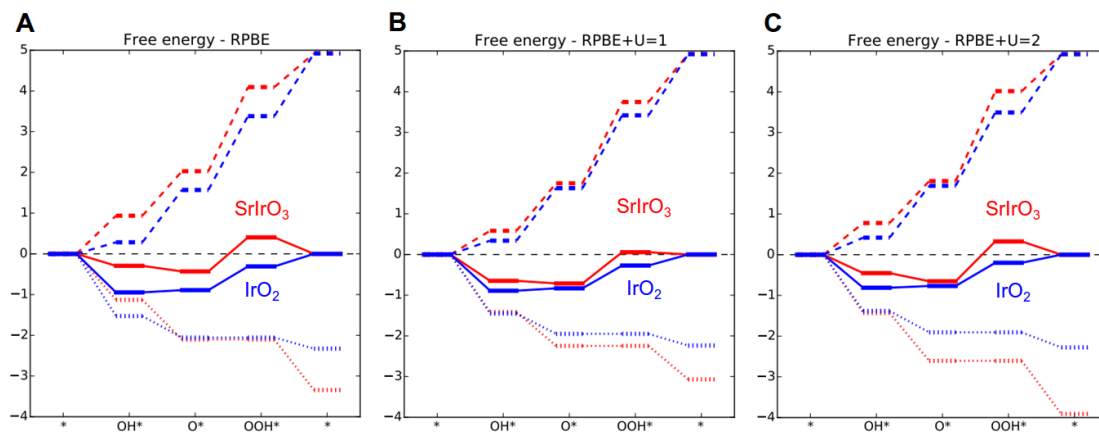


Figure 14. Calculated free energy of the OER intermediates for IrO₂ and SrIrO₃, solid line: at 1.23V vs. RHE, dashed line: at 0V vs. RHE, dotted line: at the thermodynamics overpotential. All calculations use GGA-RPBE with (A) *U* = 0 eV, (B) *U* = 1 eV, and (C) *U* = 2 eV.

Chapter 4

Summary & Outlook

In conclusion, we have studied the OER activity on a SrIrO₃(100) film grown on DyScO₃(110) substrate. We find that SrIrO₃ exhibits more than an order of magnitude of activity higher than IrO₂ despite having in the same nominal valency (Ir⁴⁺). The electrochemical behavior of SrIrO₃ is more similar to the hydrated iridium oxide than IrO₂. To our knowledge, this is the first OER activity study of SrIrO₃, demonstrating that the electrocatalytic activity of the same cation valency (Ir⁴⁺) in the same octahedral environment can depend beyond the structure beyond the octahedral. This thesis shows the utility of the advanced thin-film depositions for catalyst engineering; future uses of these advanced growth methods to create atomically tailored surface and with customized sub-surface layers can serve a new path to the design of the next-generation OER catalysts.

REFERENCES

1. Greeley, J. & Markovic, N. M., The road from animal electricity to green energy: combining experiment and theory in electrocatalysis. *Energy Environ. Sci.* **5**, 9246-9256 (2012).
2. Cook, T. R. et al., Solar Energy Supply and Storage for the Legacy and Non legacy Worlds. *Chem. Rev.* **110**, 6474-6502 (2010).
3. Cao, R., Lee, J. S., Liu, M. L., & Cho, J., Recent Progress in Non-Precious Catalysts for Metal-Air Batteries. *Adv. Energy Mater.* **2**, 816-829 (2012).
4. Peng, Z. Q., Freunberger, S. A., Chen, Y. H., & Bruce, P. G., A Reversible and Higher-Rate Li-O₂ Battery. *Science* **337**, 563-566 (2012).
5. Trasatti, S., Electrocatalysis by oxides - attempt at a unifying approach. *J. Electroanal. Chem.* **111**, 125-131 (1980).
6. Man, I. C. et al., Universality in oxygen evolution electrocatalysis on oxide surfaces. *ChemCatChem* **3**, 1159-1165 (2011).
7. Rossmeisl, J., Qu, Z. W., Zhu, H., Kroes, G. J., & Norskov, J. K., Electrolysis of water on oxide surfaces. *J. Electroanal. Chem.* **607**, 83-89 (2007).
8. Koper, M. T. M., Thermodynamic theory of multi-electron transfer reactions: Implications for electrocatalysis. *J. Electroanal. Chem.* **660**, 254-260 (2011).
9. Suntivich, J., May, K. J., Goodenough, J. B., Gasteiger, H. A., & Shao-Horn, Y., A perovskite oxide optimized for oxygen evolution catalysis from molecular orbital principles. *Science* **334**, 1383-1385 (2011).
10. Trotochaud, L., Ranney, J. K., Williams, K. N., & Boettcher, S. W., Solution-Cast Metal Oxide Thin Film Electrocatalysts for Oxygen Evolution. *J. Am. Chem. Soc.* **134**, 17253-17261 (2012).
11. Grimaud, A. et al., Double perovskites as a family of highly active catalysts for oxygen evolution in alkaline solution. *Nat. Commun.* **4**, (2013).

12. Pickrahn, K. L. et al., Active MnOx Electrocatalysts Prepared by Atomic Layer Deposition for Oxygen Evolution and Oxygen Reduction Reactions. *Adv. Energy Mater.* **2**, 1269-1277 (2012).
13. Liang, Y. Y., Li, Y. G., Wang, H. L., & Dai, H. J., Strongly Coupled Inorganic/Nanocarbon Hybrid Materials for Advanced Electrocatalysis. *J. Am. Chem. Soc.* **135**, 2013-2036 (2013).
14. Gong, M. et al., An Advanced Ni-Fe Layered Double Hydroxide Electrocatalyst for Water Oxidation. *J. Am. Chem. Soc.* **135**, 8452-8455 (2013).
15. Chang, S. H. et al., Functional links between stability and reactivity of strontium ruthenate single crystals during oxygen evolution. *Nat. Commun.* **5**, (2014).
16. Stoerzinger, K. A., Qiao, L., Biegalski, M. D., & Shao-Horn, Y., Orientation-Dependent Oxygen Evolution Activities of Rutile IrO₂ and RuO₂. *J. Phys. Chem. Lett.* **5**, 1636-1641 (2014).
17. Hepel, T., Pollak, F. H., & O'Grady, W. E., Irreversible Voltammetric Behavior of the (100) IrO₂ Single-Crystal Electrodes in Sulfuric-Acid Medium. *J. Electrochem. Soc.* **132**, 2385-2390 (1985).
18. Xiao, D., Zhu, W. G., Ran, Y., Nagaosa, N., & Okamoto, S., Interface engineering of quantum Hall effects in digital transition metal oxide heterostructures. *Nat. Commun.* **2**, (2011).
19. Moon, S. J. et al., Dimensionality-Controlled Insulator-Metal Transition and Correlated Metallic State in 5d Transition Metal Oxides Sr_{n+1}Ir_nO_{3n+1} (n=1, 2, and infinity). *Phys. Rev. Lett.* **101**, (2008).
20. Zhao, J. G. et al., High-pressure synthesis of orthorhombic SrIrO₃ perovskite and its positive magnetoresistance. *J. Appl. Phys.* **103**, (2008).
21. Longo, J. M., Kafalas, J. A., & Arnott, R. J., Structure and properties of the high and low pressure forms of SrIrO₃. *J. Solid State Chem.* **3**, 174-& (1971).

22. Schlom, D. G., Chen, L. Q., Pan, X. Q., Schmehl, A., & Zurbuchen, M. A., A Thin Film Approach to Engineering Functionality into Oxides. *J. Am. Ceram. Soc.* **91**, 2429-2454 (2008).
23. Nie, Y. F et al., Interplay of Spin-Orbit Interactions, Dimensionality, and Octahedral Rotations in Semimetallic SrIrO₃. *Phys. Rev. Lett.* **114**, 016401 (2015).
24. Panda, S. K., Bhowal, S., Delin, A., Eriksson, O., & Dasgupta, I., Effect of spin orbit coupling and Hubbard U on the electronic structure of IrO₂. *Phys. Rev. B* **89**, 155102 (2014).
25. Ryden, W. D., Lawson, A. W., & Sartain, C. C., Temperature dependence of the resistivity of RuO₂ and IrO₂. **26**, 209-210 (1968).
26. Lin, J. J. et al., Low temperature electrical transport properties of RuO₂ and IrO₂ single crystals. **16**, 8035 (2004).
27. Garcia-Mota, M. et al., Importance of Correlation in Determining Electrocatalytic Oxygen Evolution Activity on Cobalt Oxides. *J. Phys. Chem. C* **116**, 21077-21082 (2012).
28. Xu, Z., Rossmeisl, J., & Kitchin, J. R., A Linear Response DFT+U Study of Trends in the Oxygen Evolution Activity of Transition Metal Rutile Dioxides. **119**, 4827-4833 (2015).
29. Blakemore, J. D. et al., Comparison of Amorphous Iridium Water-Oxidation Electrocatalysts Prepared from Soluble Precursors. *Inorg. Chem.* **51**, 7749-7763 (2012).
30. Steegstra, P., Busch, M., Panas, I., & Ahlberg, E., Revisiting the Redox Properties of Hydrous Iridium Oxide Films in the Context of Oxygen Evolution. *J. Phys. Chem. C* **117**, 20975-20981 (2013).
31. Steegstra, P. & Ahlberg, E., Influence of oxidation state on the pH dependence of hydrous iridium oxide films. *Electrochim. Acta* **76**, 26-33 (2012).

32. Zhao, Y. X., Vargas-Barbosa, N. M., Hernandez-Pagan, E. A., & Mallouk, T. E., Anodic Deposition of Colloidal Iridium Oxide Thin Films from Hexahydroxyiridate(IV) Solutions. *Small* **7**, 2087-2093 (2011).
33. Strmcnik, D. et al., The role of non-covalent interactions in electrocatalytic fuel-cell reactions on platinum. *Nature Chem.* **1**, 466-472 (2009).
34. Suntivich, J., Perry, E. E., Gasteiger, H. A., & Shao-Horn, Y., The Influence of the Cation on the Oxygen Reduction and Evolution Activities of Oxide Surfaces in Alkaline Electrolyte. *Electrocatalysis* **4**, 49-55 (2013).
35. Gisbert, R., Garcia, G., & Koper, M. T. M., Adsorption of phosphate species on poly-oriented Pt and Pt(111) electrodes over a wide range of pH. *Electrochim. Acta* **55**, 7961-7968 (2010).
36. van der Niet, M. J. T. C., Garcia-Araez, N., Hernandez, J., Feliu, J. M., & Koper, M. T. M., Water dissociation on well-defined platinum surfaces: The electrochemical perspective. *Catal. Today* **202**, 105-113 (2013).
37. Sheng, W. et al., Correlating hydrogen oxidation and evolution activity on platinum at different pH with measured hydrogen binding energy. *Nat. Commun.* **6**, (2015).
38. Stoerzinger, K. A. et al., Oxygen electrocatalysis on (001)-oriented manganese perovskite films: Mn valency and charge transfer at the nanoscale. *Energy Environ. Sci.* **6**, 1582-1588 (2013).
39. Lee, Y., Suntivich, J., May, K. J., Perry, E. E., & Shao-Horn, Y., Synthesis and activities of rutile IrO₂ and RuO₂ nanoparticles for oxygen evolution reaction electrocatalysis. *J. Phys. Chem. Lett.* **3**, 399-404 (2012).
40. Bockris, J.O. & Otagawa, T., Mechanism of oxygen evolution on perovskites. *J. Phys. Chem.* **87**, 2960-2971 (1983).
41. Bockris, J.O. & Otagawa, T., The Electrocatalysis of Oxygen Evolution on Perovskites. *J. Electrochem. Soc.* **131**, 290-302 (1984).

42. Bediako, D. K., Surendranath, Y., & Nocera, D. G., Mechanistic Studies of the Oxygen Evolution Reaction Mediated by a Nickel-Borate Thin Film Electrocatalyst. *J. Am. Chem. Soc.* **135**, 3662-3674 (2013).
43. Norskov, J. K., Bligaard, T., Rossmeisl, J., & Christensen, C. H., Towards the computational design of solid catalysts. *Nature Chem.* **1**, 37-46 (2009).
44. Choy, J. H., Kim, D. K., Hwang, S. H., Demazeau, G., & Jung, D. Y., XANES and EXAFS Studies on the Ir-O Bond Covalency in Ionic Iridium Perovskites *J. Am. Chem. Soc.* **117**, 8557-8566 (1995).
45. Bolzan, A. A., Fong, C., Kennedy, B. J., & Howard, C. J., Structural studies of rutile-type metal dioxides. *Acta Crystallogr. Sect. B-Struct. Commun.* **53**, 373-380 (1997).
46. Calle-Vallejo, F. et al., Number of outer electrons as descriptor for adsorption processes on transition metals and their oxides. *Chem. Sci.* **4**, 1245-1249 (2013).
47. Zeb, M. A. & Kee, H. Y., Interplay between spin-orbit coupling and Hubbard interaction in SrIrO₃ and related *Pbnm* perovskite oxides. *Phys. Rev. B* **86**, (2012).
48. May, K. J. et al., Influence of Oxygen Evolution during Water Oxidation on the Surface of Perovskite Oxide Catalysts. *J. Phys. Chem. Lett.* **3**, 3264-3270 (2012).
49. Tsymbal, Evgeny Y. et al., Multifunctional Oxide Heterostructures.
50. Walter, Michael G., et al. Solar water splitting cells. *Chemical reviews* 110.1 (2010): 6446-6473.
51. Berger, Robert F., Craig J. Fennie, and Jeffrey B. Neaton. Band Gap and Edge Engineering via Ferroic Distortion and Anisotropic Strain: The Case of SrTiO₃. *Physical review letters* 107.14 (2011): 146804.